CrossMark

ORIGINAL PAPER

Microseismic Monitoring and 3D Finite Element Analysis of the Right Bank Slope, Dagangshan Hydropower Station, during Reservoir Impounding

Xingzong Liu[1] · Chun'an Tang[1] · Lianchong Li[1] · Pengfei Lv[2] · Hongyuan Liu[3]

Abstract The right bank slope of Dagangshan hydropower station in China has complex geological conditions and is subjected to high in situ stress. Notably, microseismic activities in the right bank slope occurred during reservoir impounding. This paper describes the microseismic monitoring technology, and three-dimensional (3D) finite element analysis is used to explore the microseismic activities and damage mechanisms in the right bank slope during reservoir impounding. Based on data obtained from microseismic monitoring, a progressive microseismic damage model is proposed and implemented for 3D finite element analysis. The safety factor for the right bank slope after reservoir impoundment obtained from the 3D finite element analysis, which included the effects of progressive microseismic damage, was 1.10, indicating that the slope is stable. The microseismic monitoring system is able to capture the slope disturbance during reservoir impounding in real time and is a powerful tool for qualitatively assessing changes in slope stability over time. The proposed progressive microseismic damage model adequately simulates the changes in the slope during the impoundment process and provides a valuable tool for evaluating slope stability.

List of symbols

D	Damage variable
E	Elastic modulus
K	Safety factor
M	Moment tensor
$\dot{M}$	The rate of the moment tensor
RFPA-3D	3D realistic failure process analysis
S_{tep}	Load step
U^{e}	Total releasable elastic strain energy
U_{M}	Radiation energy
V	Structure block volume
Δg	Centrifugal loading coefficient
ΔU	Actual assigned energy
γ	Material unit weight
$\dot{\varepsilon}_1$	Principal extension strain rate
$\dot{\varepsilon}_2$	Principal contraction strain rate
$\dot{\bar{\varepsilon}}$	Mean strain rate
η	Seismic efficiency
μ	Shear modulus
v	Poisson's ratio
σ	Compressive strength
t	Time interval

✉ Chun'an Tang
tca@mail.neu.edu.cn

[1] State Key Laboratory of Coastal and Offshore Engineering, Dalian University of Technology, Dalian 116024, China

[2] Guodian Dadu River Dagangshan Hydropower Development Co., Ltd., Ya'an 625409, China

[3] School of Engineering and ICT, University of Tasmania, TAS 7005, Australia

1 Introduction

Instantaneous and progressive failures are two important instability mechanisms in rock slopes. The former refers to landslides that occur when all points on the slope slip surface are simultaneously at their ultimate state. For most

slopes, due to the inhomogeneous stress and strain distributions on the slip surface and discontinuous surfaces such as faults, different failure probabilities occur at different locations on the slip surface; thus, slope failure becomes a progressive process (Yang et al. 2005). The concept of progressive slope failure was originally introduced to explain the discrepancies between the back-calculated average shear stresses along failure surfaces in overconsolidated clay slopes and the shear strength of the same clay material experimentally obtained in laboratory tests. Bjerrum (1967) indicated that slides in overconsolidated clay and clay shale slopes are preceded by the progressive development of a continuous sliding surface. However, one of the earliest descriptions of progressive slope failure was given in 1963, when a catastrophic landslide occurred on the upstream slope of the Vajont dam in Italy (Barla and Paronuzzi 2013). The Vajont landslide was attributed to a reduction in peak shear strength during the impoundment process of the reservoir; therefore, the progressive failure mechanism can explain the Vajont landslide (Chowdhury 1978). Additionally, long-term rock slope observations have indicated that most slope instabilities involve a gradual and intermittent displacement mechanism.

Currently, theoretical analysis, laboratory testing and numerical simulations are the main methods used to study progressive slope failure. Gencer (1985) and Miao et al. (2011) established theoretical models to analyse the progressive failure of slopes. In the laboratory, centrifuge testing has been widely used to study progressive slope failure (Adhikary and Dyskin 2007; Wang and Zhang 2014). In addition, Zhu et al. (2011) conducted a series of physical model tests to better understand the behaviour of progressive slope failure. The finite and finite-discrete element methods (Eberhardt et al. 2004; Zhang et al. 2005, 2014; Gurocak et al. 2008; William et al. 2008; Tang et al. 2015), the numerical manifold method (Wong and Wu 2014) and the meshless method (Zhou et al. 2015) are the main numerical methods used to analyse progressive slope failure.

Progressive slope failure is caused by a gradual decrease in the shear strength of a rock mass. Before a landslide, the shear strength of the rock mass along the potential sliding surface must be greater than the induced stress, and the entire sliding mass must satisfy static equilibrium conditions. Only when the slope is sufficiently disturbed and the shear strength of the sliding mass is exceeded can the potential sliding surface cut through the entire slope and cause a landslide. The causes of progressive slope failure can be roughly divided into two categories: internal causes, such as gravity (Chen et al. 2013), and external causes, such as intense rainfall (Hong et al. 2005; Borja and White 2010; Ma et al. 2014; Igwe et al. 2014), earthquake activity (Wang et al. 2010; Parker et al. 2013; Gischig et al. 2016), changes in water level (Xiao et al. 2007; Liao et al. 2005; Wang et al.

2013) and artificial disturbances (Leshchinsky et al. 2015; Dai et al. 2004; Cheng et al. 2012; Zhao et al. 2014).

Several major hydropower engineering projects have been implemented in south-western China over the past decade due to the abundant water resources present in this area; as a result, many high and steep slopes have been formed in reservoir construction. Steep slopes resist dam thrust forces and are influenced by the construction and operation of high dams. Whether a dam can undergo impoundment is a key question in slope safety (Lin et al. 2015; Tomida et al. 2011; Zhou et al. 2013). The abutment slopes are strongly influenced by the water-level changes that occur during reservoir impounding, and the slope stability can significantly decrease due to water-level changes and weak geological conditions. Chen (2010) reviewed the representative research on the progressive failure of reservoir bank slopes caused by the impounding process worldwide. Lin et al. (2016) studied the unstable rock slope in Laxiwa Reservoir and showed signs of gravitational and water-impounding-induced large deformations. Xiang and Tang (2011) discussed the landslide mechanism of a reservoir bank slope induced by water-level changes. Wang et al. (2005, 2008) conducted field investigations and tests to explore the instability mechanism of a slope in response to reservoir impoundment. In addition to theoretical analysis, field monitoring and testing, numerical modelling has been used to study slope failures caused by water-level changes (Yerro et al. 2015; Yang et al. 2013; Wang et al. 2007; Wang and Yan 2007; Xia et al. 2014; Jiao et al. 2014).

This paper focuses on the stability of the right bank slope of the Dagangshan hydropower station, which is located in Sichuan Province, China, during reservoir impounding. A microseismic monitoring system was installed in the right bank slope, and the disturbance area of the slope during the impoundment process was determined based on the detected seismic activity. A numerical method was then implemented to explore the damage mechanism in the disturbed area of the slope during the different stages of reservoir impoundment. A progressive microseismic damage model was then established using the extensive information captured by the microseismic monitoring system. The safety factor of the slope during the impoundment process was obtained using a numerical method that considers the effects of progressive microseismic damage. Finally, the stability of the slope was evaluated by analysing the slope safety factor during water storage.

2 Microseismic Monitoring of the Right Bank Slope During Reservoir Impounding

2.1 Project Overview

The Dagangshan hydropower station is located within the Huangcaoshan fault block, which is cut by the Moxi, Daduhe

and Jinping fault ruptures. The project was constructed in a V-shaped valley (Fig. 1a); the mountains on both sides of the project are very tall, and the bedrock was exposed after excavation. The right bank slope is steep, with a gradient that varies from 40° to 65° and a relative altitude difference of more than 600 m (Fig. 1a). The main rock type of the slope in the project area is medium-grained granite. Additionally, there are diabase dikes (β_5, β_{43}, β_{62}, β_{68}, β_{83} and β_{85}), fine-grained granitic dikes (γL_5, γL_6) and diorite dikes in the slope (Fig. 1b). The diabase dikes are dominant, as indicated by the green lines in Fig. 2a. Field surveys indicate that the exposed width of the diabase dikes ranges from 0.5 to 10 m on average, with a maximum width of up to 26 m. Overall, there are 203 fractured diabase dikes or diabase dikes with an exposed width of greater than 2 m, and 56 dikes are wider than 5 m. The diabase dikes predominantly dip at a steep angle.

The granite in the slope surrounding the project area primarily has a medium-grained texture with a low resistance to weathering. The diabase dike has a dense medium-grained texture with a slight weathering grade. When affected by

Fig. 1 Right bank slope of Dagangshan hydropower station. **a** The right bank slope after completing excavation. **b** Photograph of the right bank showing the geological conditions

faults, the dikes are easily weathered. Fortunately, there are no regional faults in the slope around the project area, and the main geological structures are dikes with faults, fracture zones and joint fissures. Field surveys indicate that in addition to the main dikes in the right bank slope of the Dagangshan hydropower station, the project area includes small-scale faults, as indicated by the red lines in Fig. 2a, a main fault (f231) and two large deep unloading fissure zones (XL-316 and XL-915), as depicted in Fig. 2a.

Macro-cracks appeared during slope excavation, and rock mass deformation occurred along the unloading fissure zone XL-316 and fault f231. To restrain the rock mass deformation, the weak structure blocks along fault f231 were excavated and backfilled using micro-expansion concrete to construct anti-shear galleries at elevations of 1240, 1210, 1180, 1150, 1120 and 1060 m, as shown in Fig. 2a, b.

2.2 Results of Microseismic Monitoring

Based on the project plan, the Dagangshan hydropower station was to begin storing water at the end of 2014. An advanced microseismic monitoring system was implemented in the right bank slope in November 2014 to monitor the slope disturbance during the reservoir impounding period. Nineteen sensors were arranged in an array at ten elevations along the right bank slope for long-term monitoring (Fig. 3). The monitoring area was 400 m long along the river, 400 m deep along the slope surface, and 600 m tall, covering elevations between 800 and 1400 m (i.e. 400 m × 400 m × 600 m). The monitoring data were collected and sent to a central control room located at an elevation of 1135 m (Fig. 3).

In the Dagangshan hydropower station, the water level of the reservoir was increased by 100 m from an elevation of 1020 m over a 28-day period starting on 29 May 2015. After filtering out noisy events, 51 effective microseismic events were captured by the microseismic monitoring system during water impoundment, as shown in Fig. 4. Figure 5 provides a comparison of Figs. 2a and 4 and clearly shows that the effective microseismic events captured during water impoundment were mainly distributed near the anti-shear galleries at elevations of 1240, 1210, 1180 and 1150 m and near diabase dikes β_{43}, β_{68}, β_{83} and β_{85}.

3 Damage Mechanisms Within the Right Bank Slope During Water Storage

3.1 Spatiotemporal Distributions of the Microseismic Events

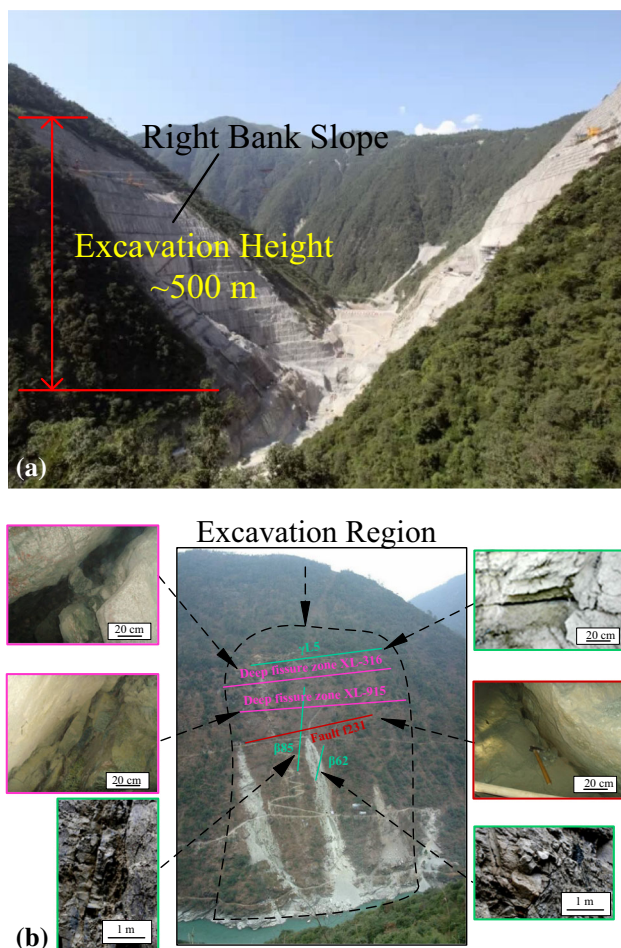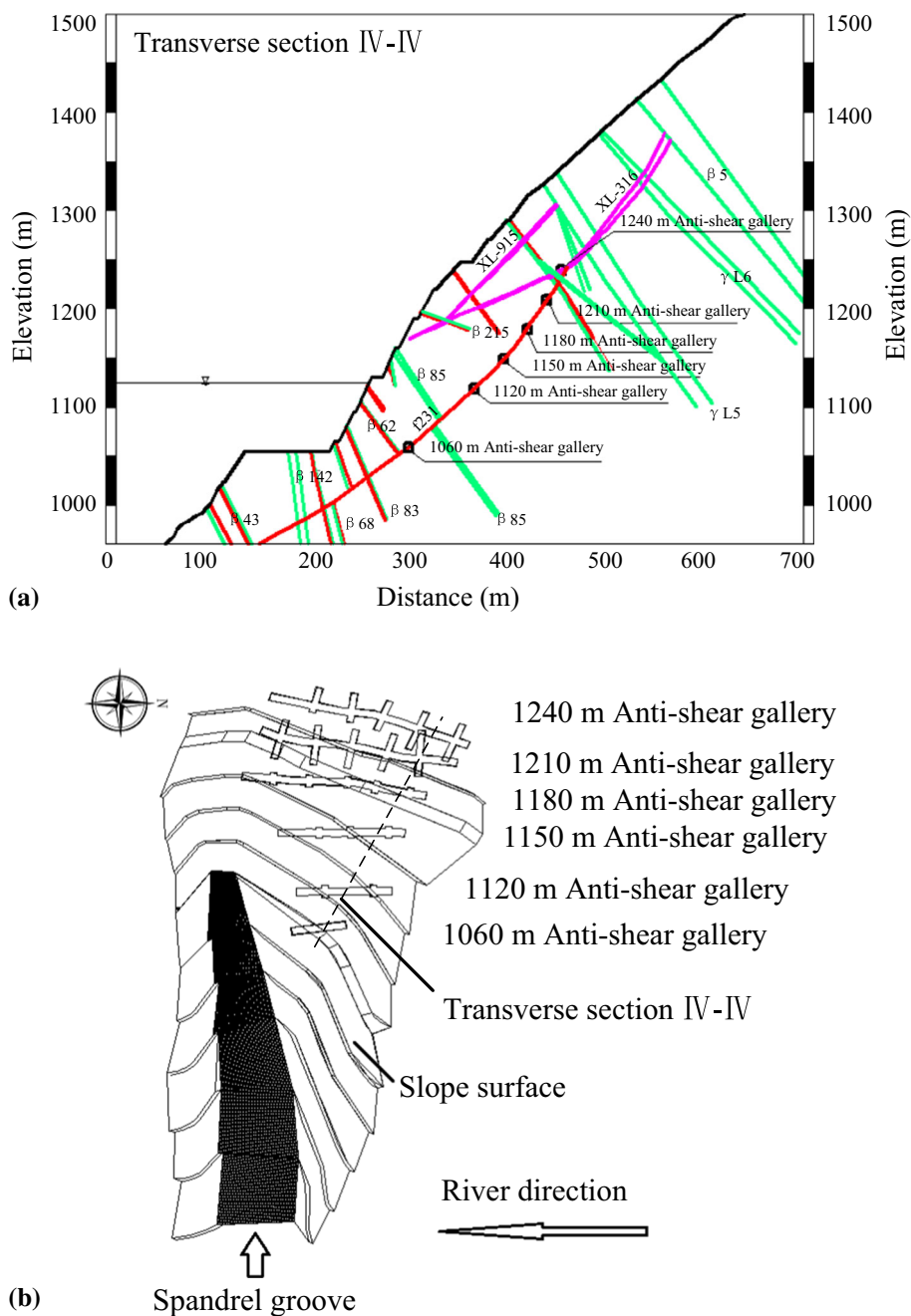A number of microseismic events occurred during the water storage period that was related to the long-term water

Fig. 2 Geotechnical model of the right bank slope with the layout of the constructed anti-shear galleries. **a** Geotechnical model of the right bank slope along a typical transverse section *IV–IV*. **b** The anti-shear galleries constructed along fault f231

storage and the distinct increase in the water level during reservoir impounding. To explore the distribution trends of the microseismic events in the right bank slope during water impoundment, the process was divided into four stages, with each stage lasting 7 days. The microseismic events monitored up to the end of each stage are depicted in Fig. 6. In this figure, each coloured circle represents a microseismic event; the size of the solid circle reflects the size of the energy released by the microseismic event; and the specific value of the released energy is represented by the colour. During the first stage, the water level of the

reservoir increased from an elevation of 1020–1040 m. Many microseismic events appeared to be associated with diabase dikes β_{68}, β_{83} and β_{85}, and a small number of events were located near the anti-shear galleries located at elevations of 1210 and 1180 m. During the following two stages, the water level increased from an elevation of 1040 to 1080 m. No additional microseismic events occurred near diabase dikes β_{68}, β_{83} and β_{85}, but a cluster of events was observed near the anti-shear galleries at elevations of 1240, 1210, 1180 and 1150 m. In the last stage of impoundment, the water level increased from an elevation

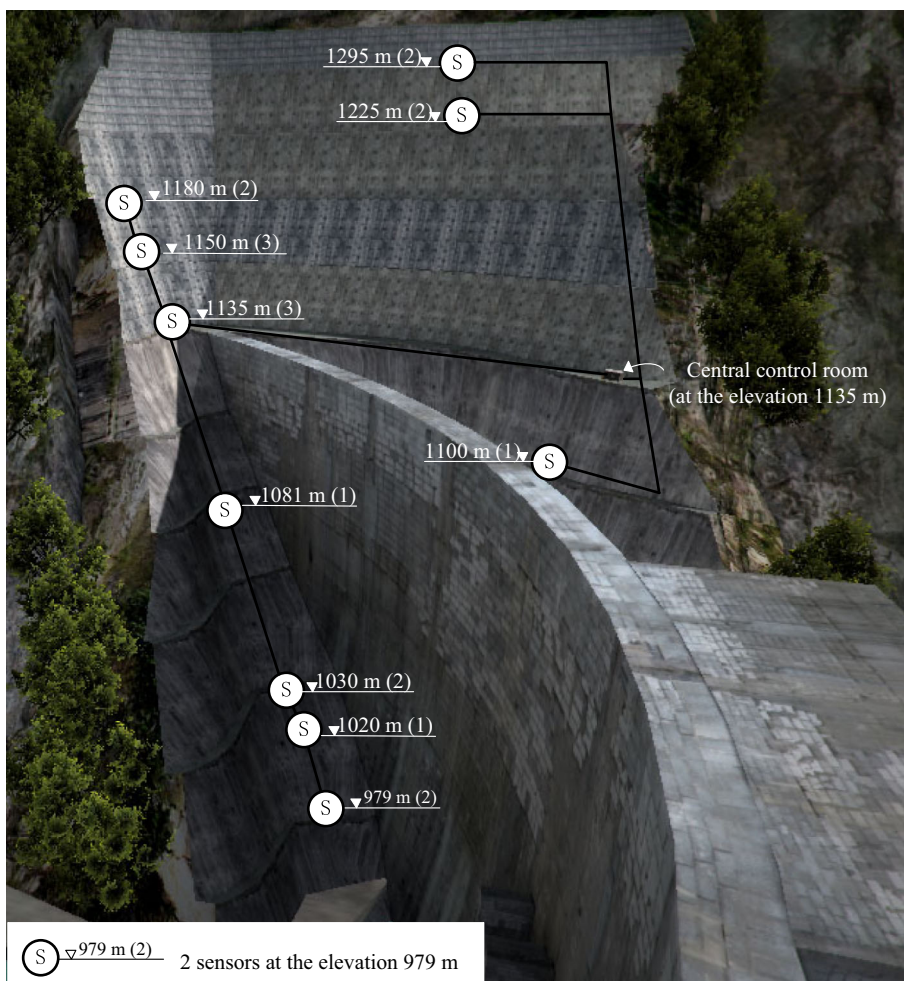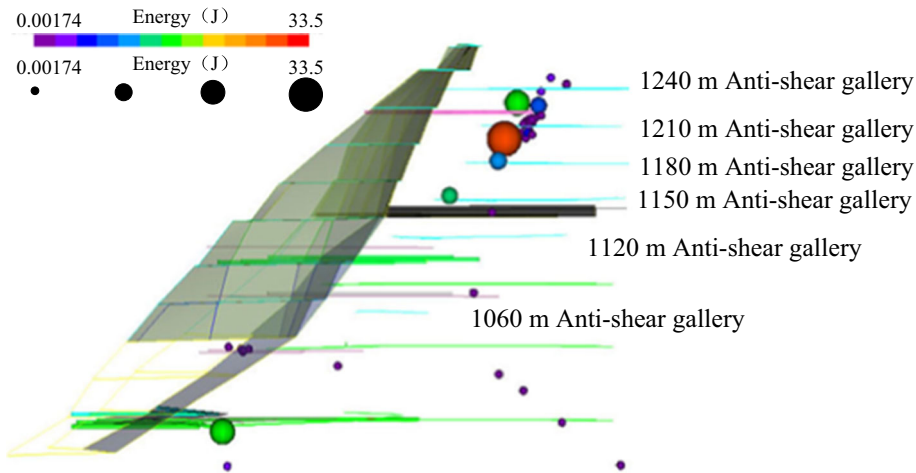**Fig. 3** Layout of the microseismic monitoring sensors

**Fig. 4** Effective microseismic events captured during impoundment

of 1080–1120 m. Major microseismic events were distributed around the anti-shear galleries at elevations of 1240 and 1210 m, whereas a few events were detected adjacent to fault f231 and diabase dike β_{43}.

In summary, the microseismic events were predominantly distributed near the anti-shear galleries and diabase dikes during the impoundment process. Moreover, the microseismic events were distributed within the rock mass at low elevations during the early stage of reservoir impoundment. With increasing water level, more microseismic events were recorded in the rock mass at high elevations. During the period of water storage, the number
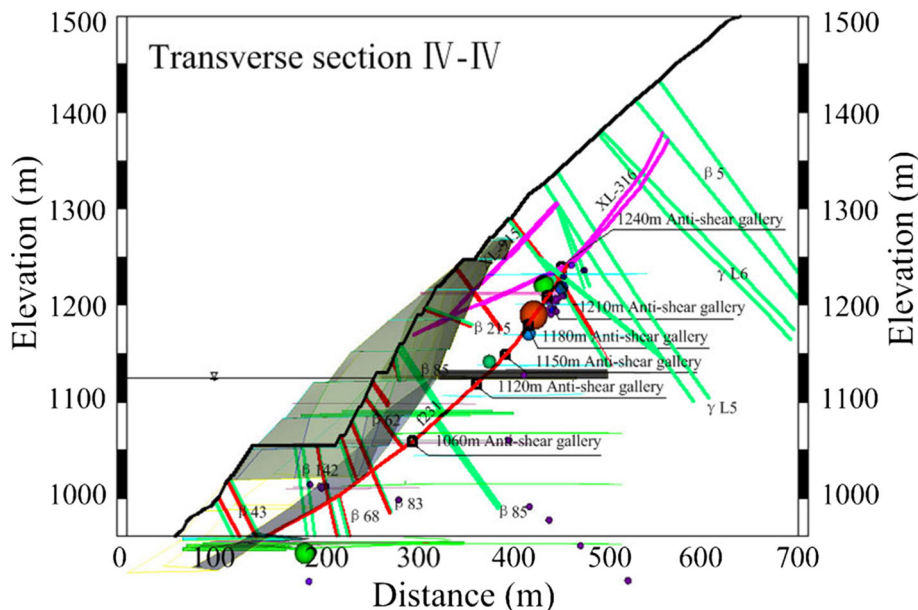
of microseismic events increased, with most events concentrated within the rock mass at high elevations.

3.2 Analysis of Seismic Deformation

Based on the spatiotemporal distribution characteristics of the monitored microseismic events, with increasing water level, the rock mass around the anti-shear galleries at high elevations was frequently displaced, and the disturbance became increasingly intense. The damage mechanism in the right bank slope during water impoundment can be understood by analysing the seismic deformation.

Jackson and McKenzie (1988) and Pondrelli et al. (1995) quantified seismic deformation based on the relationship between rock mass deformation due to seismic activities and the seismic moment tensor. Kostrov (1974) determined the relation between the average strain $\bar{\varepsilon}_{ij}$ within a volume V and the sum of the seismic moment tensors:

$$\bar{\varepsilon}_{ij} = \frac{1}{2\mu V} \sum_{k=1}^{K} M_{ij}^k \tag{1}$$

where M_{ij}^k is the ijth component of the moment tensor M of the kth event and μ is the shear modulus. If the time interval is t, then the rate of the moment tensor $\dot{M}_{ij}$ in the volume V can be written as follows:

$$\dot{M}_{ij} = \frac{1}{t} \sum_{k=1}^{K} M_{ij}^k \tag{2}$$

Correspondingly, the average strain rate is calculated according to the following equation.

$$\dot{\bar{\varepsilon}}_{ij} = \frac{\bar{\varepsilon}_{ij}}{t} = \frac{1}{2\mu V} \dot{M}_{ij} = \frac{1}{2\mu V t} \sum_{k=1}^{K} M_{ij}^k \tag{3}$$

Moreover, Savage and Simpson (1997) suggested that the minimum scalar moment rate $M_{\min}$ is equivalent to the principal strain rates $\dot{\varepsilon}_1$ and $\dot{\varepsilon}_2$ acting within the volume V:

$$M_{\min} = 2\mu V \max(|\dot{\varepsilon}_1|, |\dot{\varepsilon}_2|, |\dot{\varepsilon}_1 + \dot{\varepsilon}_2|) \tag{4}$$

where $\max(|\dot{\varepsilon}_1|, |\dot{\varepsilon}_2|, |\dot{\varepsilon}_1 + \dot{\varepsilon}_2|)$ denotes the maximum of $|\dot{\varepsilon}_1|$, $|\dot{\varepsilon}_2|$ and $|\dot{\varepsilon}_1 + \dot{\varepsilon}_2|$ and $\dot{\varepsilon}_1$ and $\dot{\varepsilon}_2$ are the principal extension and contraction strain rates, respectively.
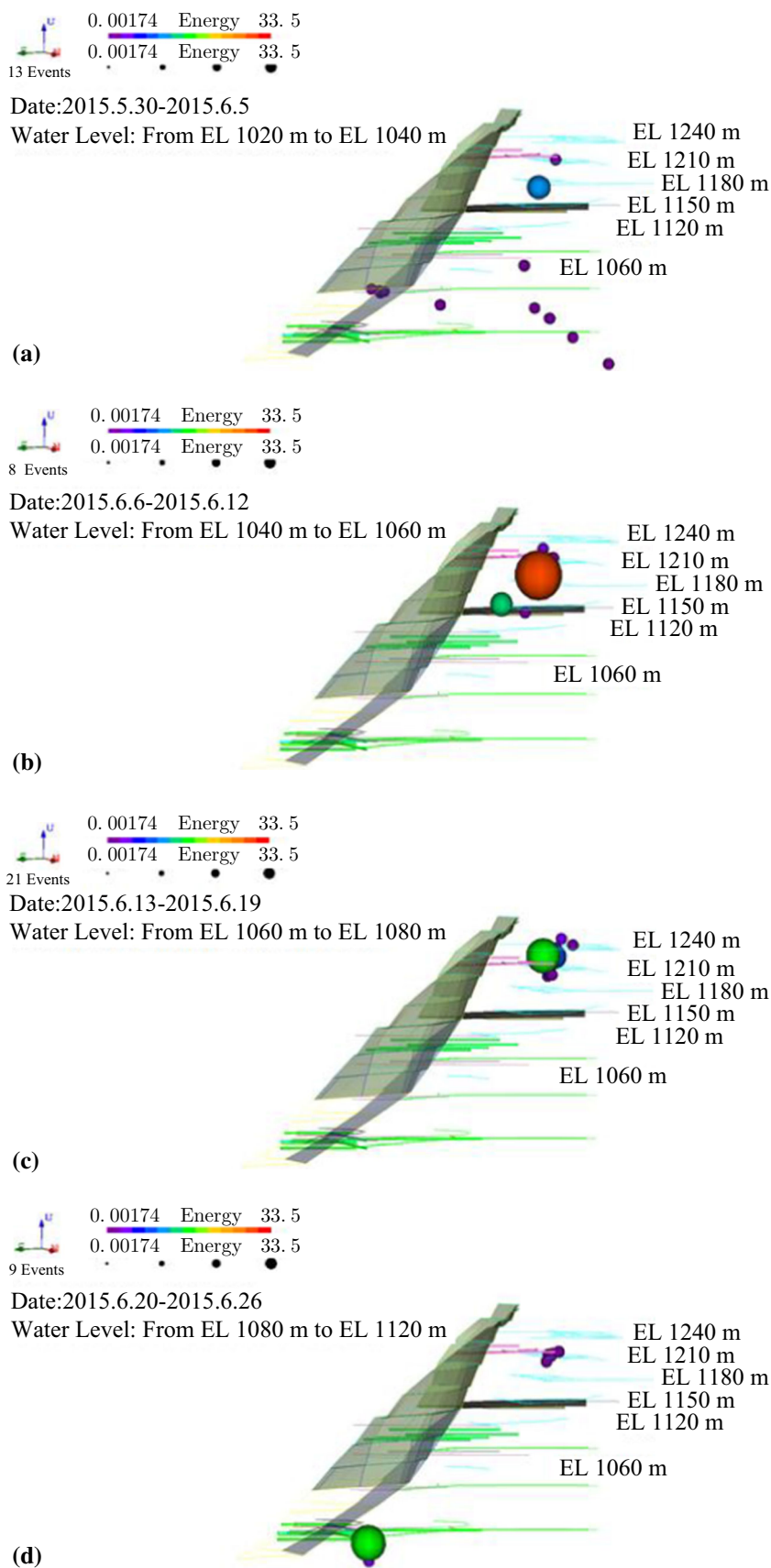
Thus, the scalar form of the mean strain rate can be written as follows:

$$\dot{\bar{\varepsilon}} = \frac{M_{\text{total}}}{2\mu V t} \tag{5}$$

where M_{total} is the total seismic moment over the time interval t.

The parameters in Eq. 5, such as the seismic moment M_{total}, the structure block volume V and the time interval t, can be obtained from seismic source data, which can be easily collected by a microseismic monitoring system. Thus, the mean strain rate can be calculated according to Eq. 5 and can then be used as an index to analyse the slope seismic deformation during water impoundment. Figure 7 illustrates the seismic deformation of the right bank slope calculated using the proposed method during the impoundment process. During the early stage of water storage, appreciable deformation is observed in the outcropping area of dikes β_{68} and β_{83}. Deformation in the anti-shear galleries at elevations of 1240, 1210, 1180 and 1150 m is not evident at a water-level elevation of 1040 m

Fig. 6 Distributions of the monitored microseismic events during the impoundment process over a period of 28 days: **a** 7 days, **b** 14 days, **c** 21 days, and **d** 28 days

13 Events

0. 00174 Energy 33. 5
0. 00174 Energy 33. 5

Date:2015.5.30-2015.6.5
Water Level: From EL 1020 m to EL 1040 m

EL 1240 m
EL 1210 m
EL 1180 m
EL 1150 m
EL 1120 m
EL 1060 m

(a)

8 Events

0. 00174 Energy 33. 5
0. 00174 Energy 33. 5

Date:2015.6.6-2015.6.12
Water Level: From EL 1040 m to EL 1060 m

EL 1240 m
EL 1210 m
EL 1180 m
EL 1150 m
EL 1120 m

EL 1060 m

(b)

21 Events

0. 00174 Energy 33. 5
0. 00174 Energy 33. 5

Date:2015.6.13-2015.6.19
Water Level: From EL 1060 m to EL 1080 m

EL 1240 m
EL 1210 m
EL 1180 m
EL 1150 m
EL 1120 m

EL 1060 m

(c)

9 Events

0. 00174 Energy 33. 5
0. 00174 Energy 33. 5

Date:2015.6.20-2015.6.26
Water Level: From EL 1080 m to EL 1120 m

EL 1240 m
EL 1210 m
EL 1180 m
EL 1150 m
EL 1120 m

EL 1060 m

(d)

(Fig. 7). With increasing water level, the deformation in the surface area of dikes β_{68} and β_{83} decreases. By contrast, in the anti-shear galleries at elevations of 1240, 1210, 1180 and 1150 m, deformation increases, and the area of deformation increases at water-level elevations of 1060, 1080 and 1120 m, as shown in Fig. 7.

By definition, the mean strain rate is proportional to the deformation rate, which is reflected in the sensitivity of the structure to external loads. Thus, according to the previously introduced evolution of seismic deformation, a rock mass block located at a low elevation in the slope deforms rapidly when the impoundment water level is low, and the deformation suddenly stops as the water level increases. Simultaneously, the rock mass surrounding the anti-shear galleries at elevations of 1240, 1210, 1180 and 1150 m is disturbed by the impoundment of water, and the disturbance continues for a long time. Correspondingly, the seismic deformation illustrated in Fig. 7 shows that although the right bank slope is reinforced by anti-shear galleries, unstable zones still exist within the slope. The zone of instability mainly comprises the rock mass surrounding the anti-shear galleries at elevations of 1240, 1210, 1180 and 1150 m; the instability in this region is greater than that at lower elevations in the slope. The

contours of energy density associated with microseismic events with increasing water level are shown in Fig. 8. Although the unstable blocks at low elevations are the first to be disturbed during water storage, the energy released by rock mass fracturing per unit volume in this region is small, and the energy density distribution in this region is similar to that in other regions. As the impoundment water level increases, the energy released by rock mass fracturing near the four upper anti-shear galleries becomes distinctly larger than that in other regions; furthermore, the rock mass fracture zone in this area tends to increase, as shown in Fig. 8. Therefore, according to the evolution of the energy density of the monitored microseismic events, the disturbance surrounding the upper four anti-shear galleries becomes more active, and the rock mass becomes more severely damaged as the impounded water level increases, which also affects nearby areas.

3.3 Exploration of Slope Damage Mechanisms Associated with Reservoir Impoundment

To investigate the slope damage mechanism during the process of water impounding, a three-dimensional (3D) numerical model was built according to the actual
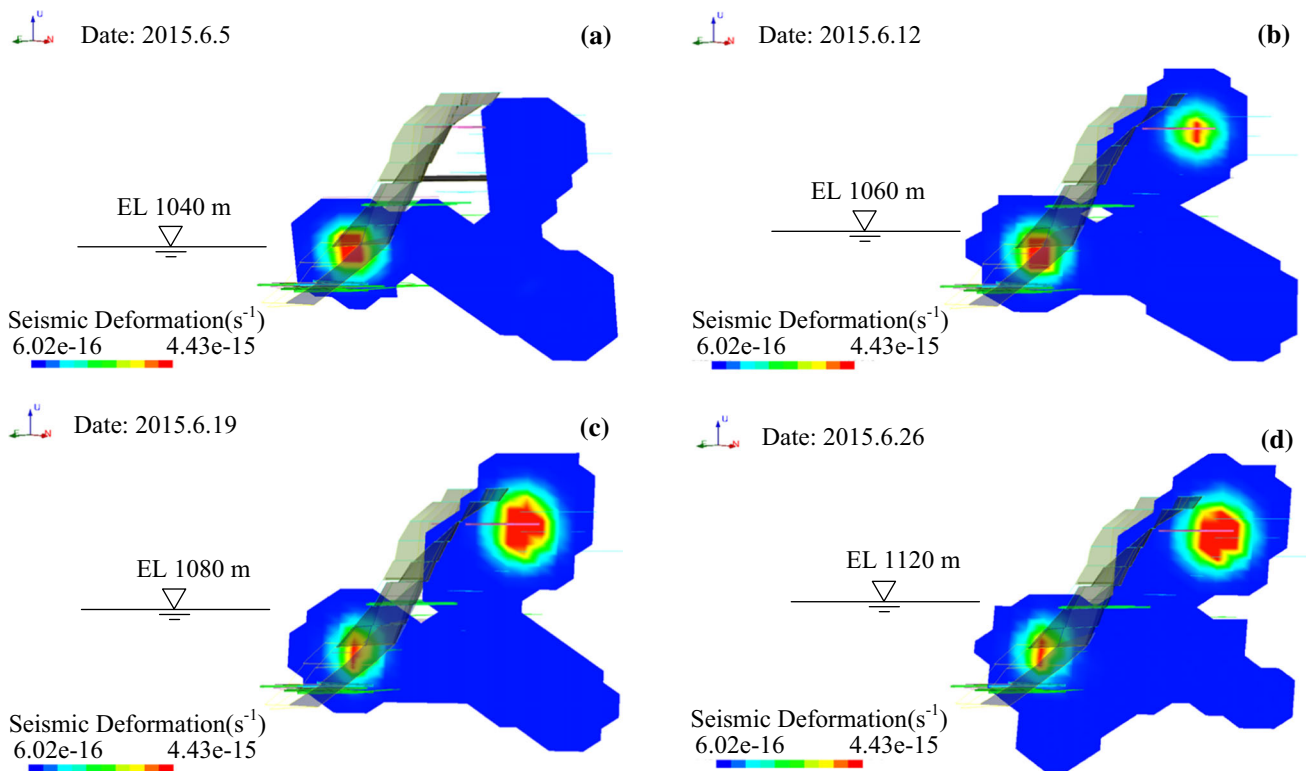

Fig. 7 Evolution of the seismic deformation of the right bank slope during the impoundment process over a period of 28 days: **a** 7 days, **b** 14 days, **c** 21 days, and **d** 28 days
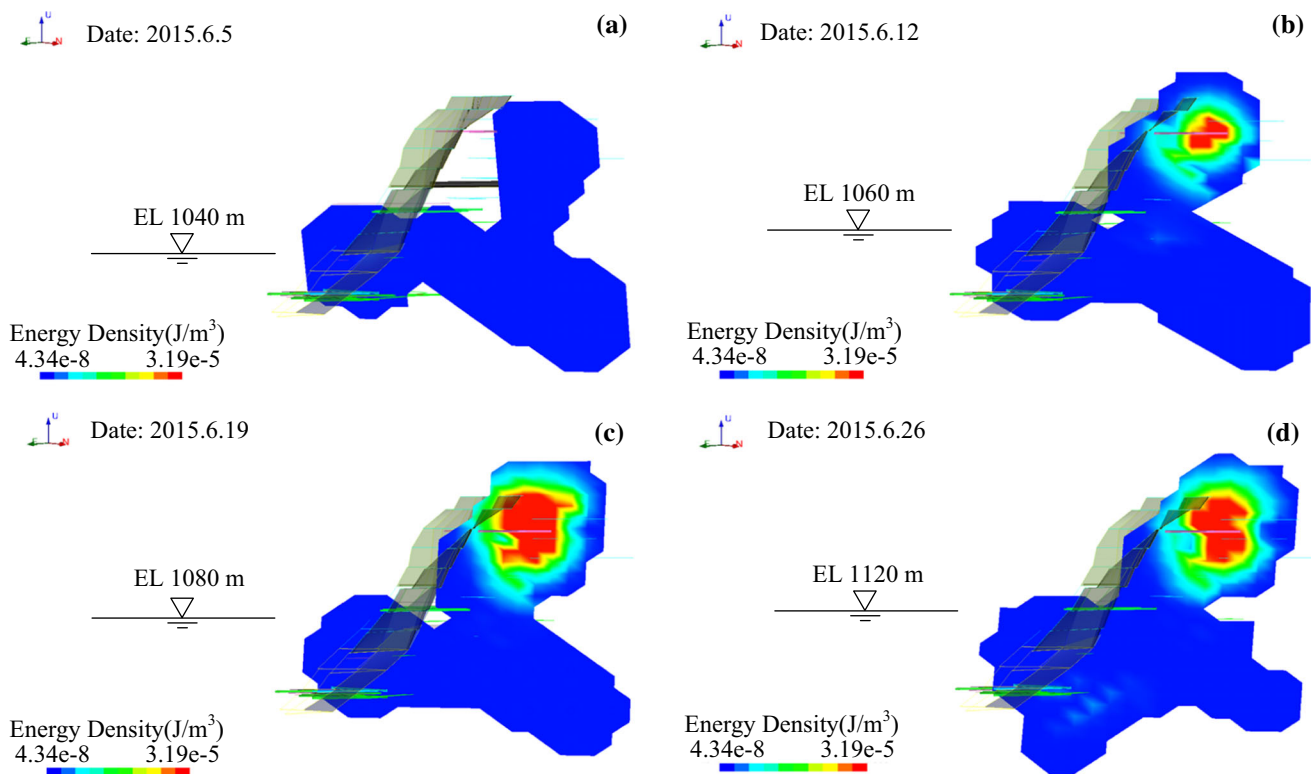
Fig. 8 Evolution of the energy density of the right bank slope during the impoundment process over a period of 28 days: **a** 7 days, **b** 14 days, **c** 21 days, and **d** 28 days

geological conditions of the right bank slope (Fig. 2a). The model has dimensions of 914 m perpendicular to the river flow direction, 400 m in the river flow direction and 720 m in the vertical direction. The simplified 3D numerical model includes the main dikes, faults, unloading fissure zones and anti-shear galleries. The commercial software ANSYS (ANSYS Manual 2000) was used to build the 3D model, which was discretized into 571,080 hexahedral finite elements and 600,700 nodes, as shown in Fig. 9. The model was restrained in the normal direction to all lateral boundaries. In addition, the bottom boundary was fixed in all three directions (x, y and z), whereas the top surface and the slope surface were free to move. The 3D finite element model was imported into a user-developed 3D realistic failure process analysis (RFPA-3D) code based on the combination of the finite element method and damage mechanics (Liang et al. 2012). This approach was then used to simulate the progressive slope failure process during water impoundment. The water load was applied to the slope surface of the model, as denoted by the box with the red dotted line in Fig. 9, and the physical and mechanical parameters of the rock masses used in the calculation are presented in Table 1.

The slope surface was reinforced by spraying concrete after excavation (Fig. 1a). Thus, it was difficult for the reservoir water to seep into the slope during impoundment.

Piezometers (Model 4500s) manufactured by Geokon were installed at elevations of 936, 948 and 950 m on the downstream right bank slope and at elevations of 1009, 1030, 1060 and 1120 m on the upstream right bank slope. Piezometric records (Fig. 10) show that the water heads at elevations of 950, 1009, 1060 and 1120 m of the right bank slope were equal to 0 metres, and the water heads at elevations of 936, 948 and 1030 m fluctuated within 2 m during the process of water impoundment. Furthermore, according to Fig. 5, the locations of most of the microseismic events were higher than the maximum water level, and the regions of concentrated microseismic events differ from the locations of water head fluctuations. Therefore, the pore water pressure has little effect on microseismic activities; only the reservoir water pressure load is considered during the impoundment process, and any seepage effects are neglected. Figure 11 illustrates the simulated results when the impoundment water level reaches an elevation of 1120 m. The rock mass damage can be described by the damage variation (Fig. 11a). A damage variation value of $D = 0$ indicates that no damage occurs, whereas a value of $D = 1$ reflects element failure. Figure 11a shows that the failure elements are mainly distributed along the unloading fissure zones XL-915 and XL-316 and fault f231; in addition, these elements are concentrated in the anti-shear galleries, whereas only a few
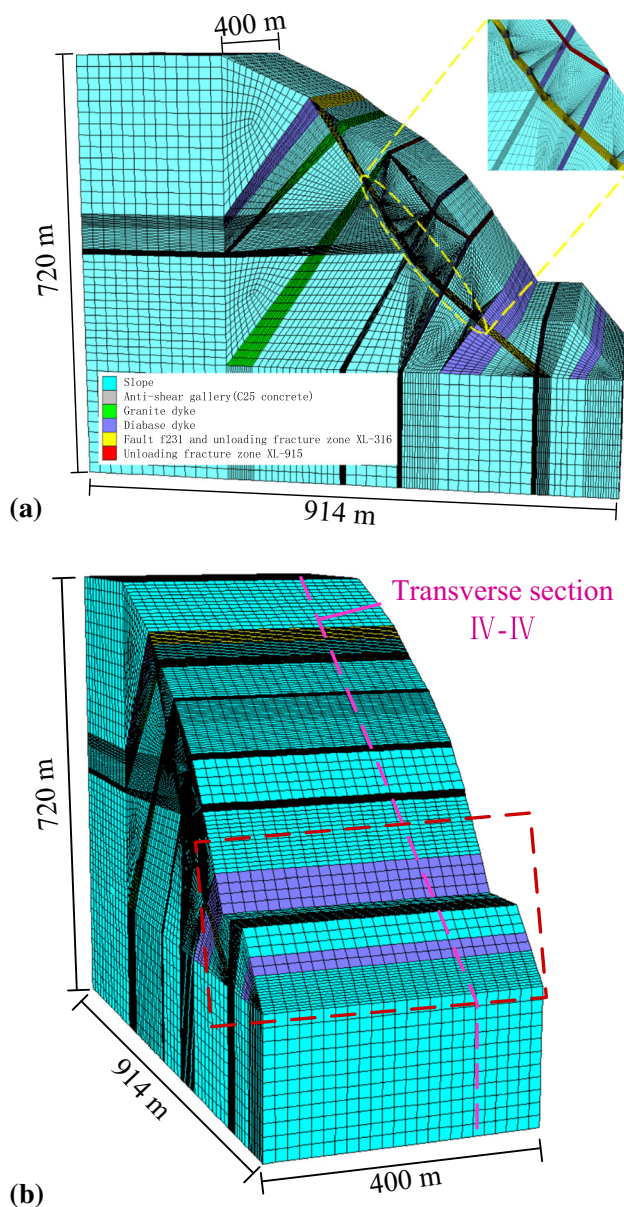
Fig. 9 Finite element model of the right bank slope from different perspectives

failed elements are distributed along dikes. The minimum principal stress contour shown in Fig. 11b indicates that the tensile stress zone covers the dikes, fissure zones, faults, anti-shear galleries, slope surface and top surface, whereas the other regions are under compression. The strength of the brittle rock mass under tension is much less than its compressive strength. Thus, the elements in the tension region are easier to damage, which explains the distribution of the failure elements shown in Fig. 11a.

Because only the reservoir water pressure load is considered during the impoundment process, the magnitude of the horizontal (x-direction) displacement is less than 10 mm (Fig. 11c). However, the displacement field within the slope is complex due to the effect of water pressure. The rock mass in the slope cut by the unloading fissure zone XL-915 tends to move. The bottom of the rock mass moves in the positive x-direction, which is towards the valley, whereas the top of the rock mass moves in the negative x-direction, which is away from the valley. Figure 11c indicates that the bottom of the rock mass surrounding unloading fissure zone XL-316 moves in the negative x-direction, whereas the top of this rock mass moves in the positive x-direction. Similarly, the bottom of the rock mass that surrounds fault f231 moves in the negative x-direction, whereas the top of this rock mass moves in the positive x-direction. Due to the complex movement behaviour of the rock mass surrounding unloading fissure zone XL-316 and fault f231, a transitional zone forms, as denoted in Fig. 11c. The top and bottom of the transitional zone move in opposite directions, with the transitional zone behaving similarly to a rock specimen in a direct shear test. The anti-shear galleries at elevations of 1240, 1210, 1180 and 1150 m are located within this transitional zone.

In summary, the numerical simulation results reflect the complex geological environment caused by unloading fissure zone XL-316, fault f231 and several dikes. Complex stress concentrations and displacements are induced in the area around the four anti-shear galleries at elevations of 1240, 1210, 1180 and 1150 m during the impoundment process. The numerical simulation also indicates that the area surrounding the anti-shear galleries at elevations of 1240, 1210, 1180 and 1150 m is the major damage region during the impoundment process. The numerical simulation results are consistent with the data obtained from the microseismic monitoring technology presented in Sect. 3.2.

Table 1 Material parameters used in the simulation

Material ID	Density (g cm^{-3})	Compressive strength (MPa)	Elastic modulus (GPa)	Poisson's ratio	Frictional angle (°)
Slope	2.65	75	21.50	0.25	48
C25 concrete	2.40	25	30.00	0.20	40
Granite dyke	2.62	30	10.00	0.27	40
Diabase dyke	2.62	30	7.50	0.30	35
XL-316 and f231	2.45	15	0.25	0.40	30
XL-915	2.10	10	0.20	0.40	30

Fig. 10 Piezometric records
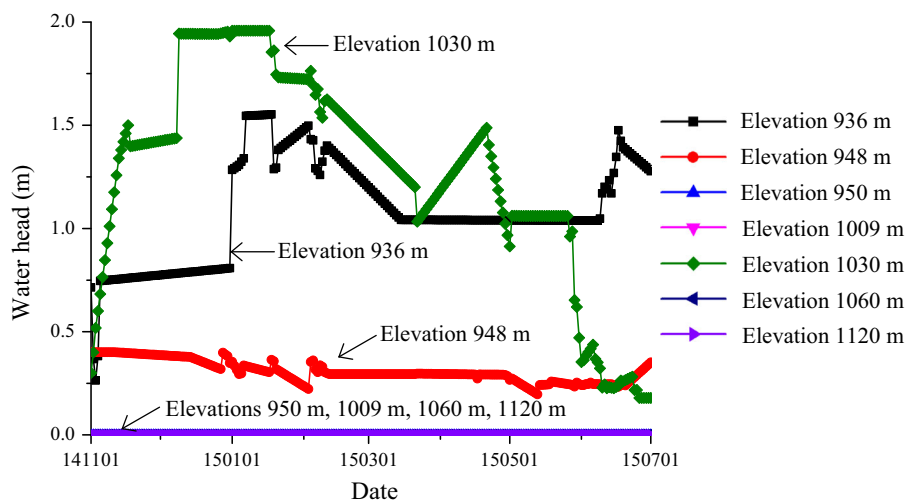
4 Analysis of Progressive Microseismic Damage in the Right Bank Slope Due to Reservoir Impoundment

As described in detail in Sects. 2 and 3, part of the rock mass in the right bank slope of the Dagangshan hydropower station moves during the impoundment process, and as the water-level rises, the location and area of the major damage in the slope gradually change. In this section, to evaluate the stability of the right bank slope during water storage, a progressive microseismic damage model is established using the information captured by the microseismic monitoring system. The 3D finite element method RFPA3D-Centrifuge (Li et al. 2009) is then used to compute the safety factor of the right bank slope during impoundment, which is used to evaluate the stability of this slope during impoundment.

4.1 RFPA3D-Centrifuge

In RFPA3D-Centrifuge, the material properties of the numerical model are held constant, and the weight is gradually increased (as in a centrifuge test) until the model fails. Elastic–plastic and elastic damage models, as introduced by Li et al. (2009), are implemented in RFPA3D-Centrifuge. Prior to reaching the failure criterion, the elements in the model remain elastic. When the failure criterion is satisfied, the element fails, and its material parameters are changed to residual values. The Mohr–Coulomb criterion with tensile strain truncation is used as the failure threshold for the elements under compression in RFPA3D-Centrifuge. If the maximum tensile stress of an element under tension reaches the tensile strength, the element becomes damaged. During the numerical simulation, a rock slope will become unstable when a complete slip surface is formed, and the corresponding safety factor K is defined as the ratio of the self-weight of the element at failure to that in its initial state:

$$K = \frac{\gamma + \gamma(S_{\text{tep}} - 1)\Delta g}{\gamma} = 1 + (S_{\text{tep}} - 1)\Delta g \qquad (6)$$

where S_{tep} is the loading step when the slope fails; Δg is the centrifugal loading coefficient, which represents the increased percentage of the material weight in each loading step; and γ is the material unit weight. In RFPA3D-Centrifuge, the heterogeneity of geological materials is considered by assuming that the mechanical properties, such as the elastic modulus and the strength, follow the Weibull distribution (Li et al. 2009). Considering the model and parameter uncertainty, each safety factor calculation was performed five times for each group of materials, and the average of the five results was taken as the safety factor.

4.2 Microseismic Damage Model

Based on the theory that energy release and dissipation during the damage process in rock are related to the rock strength (Xie et al. 2005), Xu et al. (2014) developed a microseismic damage model to evaluate the slope stability. The damage variable D of the rock mass can be defined as the ratio of the actual assigned energy ΔU of the rock mass element to the total releasable elastic strain energy U^{e}. The actual assigned energy ΔU can be calculated according to the radiation energy U_{M} and the seismic efficiency η. Thus, the damage variable D can be calculated as follows:

$$D = \frac{\Delta U}{U^{\text{e}}} = \frac{U_{\text{M}}/\eta}{U^{\text{e}}} = \frac{U_{\text{M}}}{\eta U^{\text{e}}} \qquad (7)$$

where U_{M} can be obtained from seismic source information; η is 0.001%, as obtained by blasting tests (Xu et al. 2014) on the right bank slope of Dagangshan hydropower station; and U^{e} can be calculated using Eq. 8 if the initial elastic modulus E_0, Poisson's ratio v, and the three principal stresses of the rock mass are known.
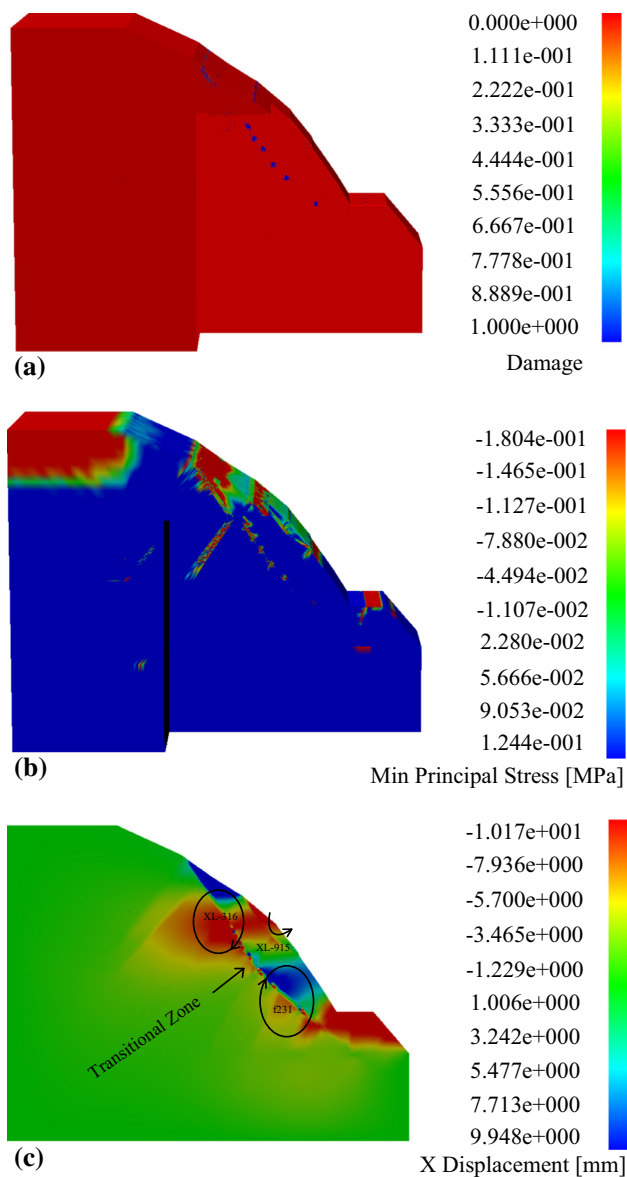
(a)

Damage

0.000e+000
1.111e-001
2.222e-001
3.333e-001
4.444e-001
5.556e-001
6.667e-001
7.778e-001
8.889e-001
1.000e+000

(b)

Min Principal Stress [MPa]

-1.804e-001
-1.465e-001
-1.127e-001
-7.880e-002
-4.494e-002
-1.107e-002
2.280e-002
5.666e-002
9.053e-002
1.244e-001

(c)

X Displacement [mm]

-1.017e+001
-7.936e+000
-5.700e+000
-3.465e+000
-1.229e+000
1.006e+000
3.242e+000
5.477e+000
7.713e+000
9.948e+000

Fig. 11 Numerical results obtained for the right bank slope during impoundment (only part of the model is depicted to clearly illustrate the distributions of the damaged elements and the minimum principal stress among all the anti-shear galleries). **a** Distribution of the damaged elements, **b** distribution of the minimum principal stress (a negative value represents tensile stress), and **c** distribution of the displacement in the *x*-direction in a typical section that includes all the anti-shear galleries

$$U^{e} = \frac{1}{2E_0}[\sigma_1^2 + \sigma_2^2 + \sigma_3^2 - 2v(\sigma_1\sigma_2 + \sigma_2\sigma_3 + \sigma_1\sigma_3)] \quad (8)$$

4.3 Progressive Microseismic Damage Analysis

Slopes are unstable if the stress state satisfies the failure criterion. In the case of partial failure, the stress state varies within the slope, and the safety factor of the slope also varies. Reservoir impoundment is a long-term process, and

failures within the slope during the process do not occur simultaneously. Progressive microseismic damage should be considered when evaluating the stability of a slope during impoundment. When the safety factor of the right bank slope of the Dagangshan hydropower station is calculated using RFPA3D-Centrifuge during the impoundment period, the seepage effect and pore pressures are neglected. The microseismic events monitored during the impoundment process are again divided into four stages, and the seismic source information in each stage is processed individually and stored in four independent files; the files are then used in the safety factor calculation, which includes the effect of microseismic damage. To fully reflect the progressive damage and the changes in slope stability during the impoundment process, the material parameters used in the earlier stages of the safety factor calculation are adjusted to include the effects of microseismic damage for use in the later stages. For example, the material parameters used in stage two are determined based on the effects of microseismic damage recorded in stage one. If an element is not damaged in stage one, its initial material parameters are used in the second calculation stage. However, if the element is damaged in stage one, then the material parameters used in stage two are adjusted according to the following equations:

$$E_1 = (1 - D)E_0 \quad (9)$$

$$\sigma_1 = (1 - D)\sigma_0 \quad (10)$$

$$v_1 = (1 + D)v_0 \quad (11)$$

where D is the damage factor of the element damaged in the previous stage; E_0, σ_0 and v_0 represent the initial elastic modulus, compressive strength and Poisson's ratio, respectively; and E_1, σ_1 and v_1 represent the elastic modulus, compressive strength and Poisson's ratio in the current stage after considering the effects of microseismic damage. To consider progressive microseismic damage, the damage factor changes in different stages according to the microseismic events, and the material parameters in each stage change accordingly. For example, the material parameters of the major damage regions in each stage are listed in Table 2.

The finite element model shown in Fig. 9 was used to calculate the safety factor of the slope during the impoundment process. In the numerical model, the centrifugal loading coefficient was set to 1%. Figures 12 and 13 illustrate the distributions of the maximum principal stress and the damage elements, respectively. The model used the centrifugal loading method for the fourth stage of the monitored microseismic events to explain the failure process of the right bank slope. Figure 12 shows that the tensile stresses in the regions of the dikes, faults, unloading fissure zones and anti-shear

Table 2 Material parameters of the major damage region in each stage

Stage ID	Compressive strength (MPa)	Elastic modulus (GPa)	Poisson's ratio
1	25.00	30.00	0.200
2	24.76	29.49	0.202
3	24.33	29.20	0.206
4	24.09	28.90	0.208

galleries are greater than those in other regions; in addition, failure initially occurs in areas with high tensile stress. Two main slip surfaces exist in the right bank slope: One is the slip surface along unloading fissure zone XL-915, and the other comprises unloading fissure zone XL-316 and fault f231. Both slip surfaces form at the top of the slope and gradually extend to the toe of the slope with the accumulation of damaged elements. Because no reinforcement measures are installed in the unloading fissure zone XL-915, the integrated slip surface forms in calculation step 11, as shown in Fig. 13. However, because of the anti-shear galleries surrounding unloading fissure zone XL-316 and fault f231, the slip surface formed there does not cut through the anti-shear galleries in calculation step 11, as illustrated in Fig. 13. According to the finite element modelling, which incorporates the effects of progressive microseismic damage, and using Eq. 6, the safety factor of the slope is calculated to be 1.10. The safety factors of the four stages obtained using the numerical modelling that considers progressive microseismic damage effects are listed in Table 3. According to Table 3, the safety factor of the slope is 1.10 during the impoundment process; because this value is greater than 1.0, the right bank slope of the Dagangshan hydropower station is generally stable during reservoir impounding. Moreover, the numerical results for step 6, as depicted in Fig. 13, show that the damaged elements are mainly distributed along the main dikes (β_{43}, β_{68}, β_{83} and β_{85}), sliding surface XL-915 and the upper part of sliding surface XL-316/f231 in accordance with the distribution of microseismic events captured by the microseismic monitoring system (Fig. 5). According to the centrifugal loading method, the slope becomes unstable in calculation step 11; however, the distribution of microseismic events during impoundment agrees with the distribution of damage elements in calculation step 6, which again indicates that the slope remains stable during impoundment.

The factors obtained from the numerical modelling that considers the effects of progressive microseismic damage are plotted in Fig. 14 together with the change in the microseismic event energy during impoundment. Table 3
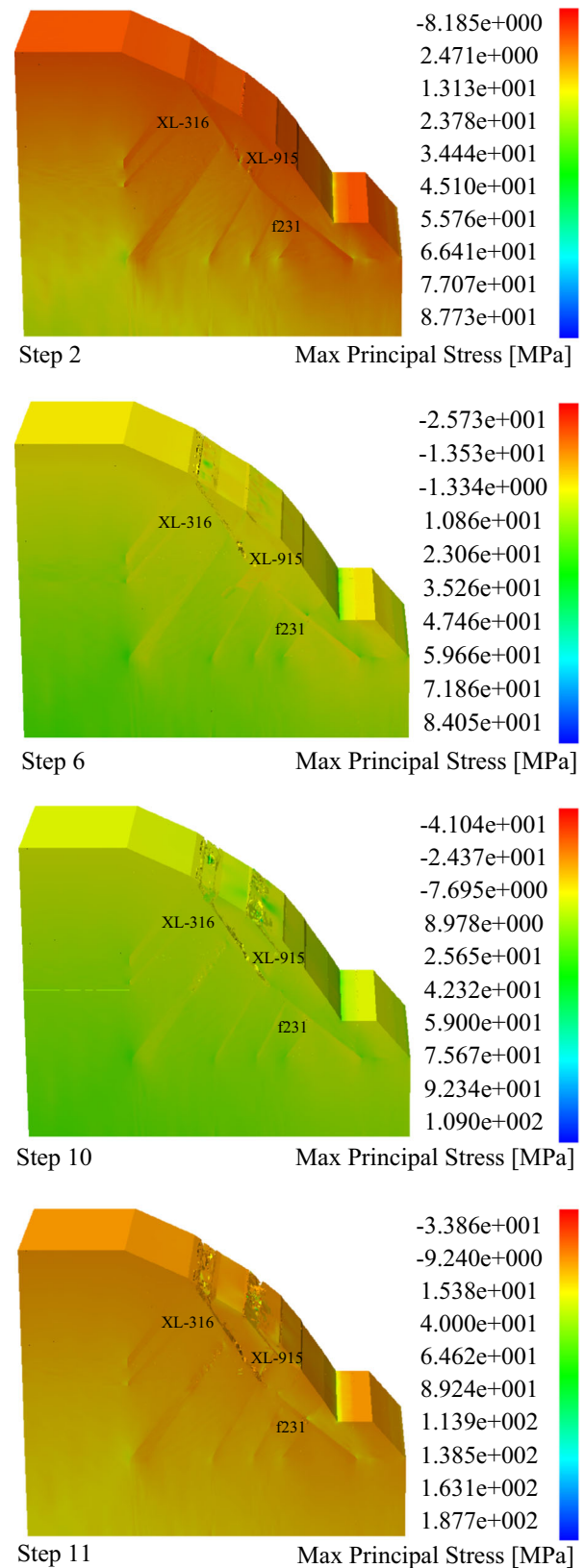

Fig. 12 Modelled failure process in the right bank slope in terms of the distribution of the maximum principal stress (a negative value represents tensile stress)
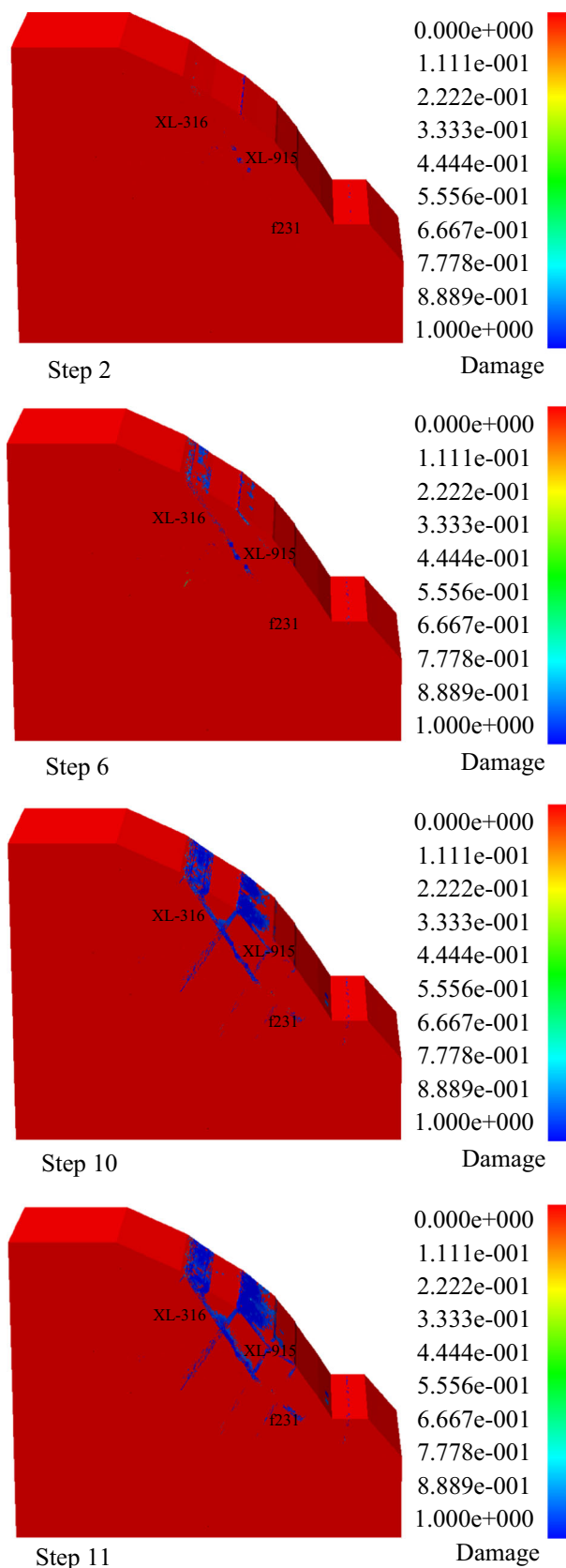
Fig. 13 Modelled failure process in the right bank slope in terms of the distribution of the damaged elements

and Fig. 14 show that the safety factor decreases as the water level increases, indicating that water storage has an adverse effect on slope stability. Moreover, the safety factor initially decreases quickly but then decreases slowly, which is related to the energy released by the microseismic events during each stage. Figure 14 clearly shows that the event with the largest energy appears in the second stage; correspondingly, the safety factor also decreases in this stage. As the event energy in the other impoundment stages is relatively small, no sudden decrease in the safety factor occurs in the other stages, which demonstrates the suitability of the proposed microseismic damage model for evaluating the slope stability. Slopes are considered unstable if the stress state satisfies the failure criterion. In the case of partial failure, the stress state varies within the slope, and the safety factor of the slope also varies. Additionally, the progressive microseismic damage considers the changes in the slope due to damage. The proposed progressive microseismic damage model provides a valuable tool for evaluating slope stability during reservoir impounding.

5 Conclusions

Microseismic monitoring technology can provide abundant seismic source information in regions of slope disturbance during reservoir impounding. In this study, the spatiotemporal distribution characteristics of monitored microseismic events are used to determine the distribution of and changes in slope disturbance in the right bank slope of the Dagangshan hydropower station during reservoir water storage. The seismic deformation reflected by monitored microseismic events demonstrates the sensitivity of the slope disturbance region. Furthermore, the combination of seismic deformation and energy density of the monitored microseismic events can be used to delineate the major damage regions in the slope during impoundment.

A 3D finite element model was built to calculate the stress and deformation in the right bank slope during the impoundment process. An analysis of slope displacement shows that the anti-shear galleries at elevations of 1240, 1210, 1180 and 1150 m and the surrounding rock mass are situated in a transitional zone. The top and bottom of the transitional zone move in opposite directions, indicating that the transitional zone is similar to a specimen experiencing direct shear. Numerical simulation reveals why the rock mass in the major damage region of the slope moves frequently, and a combination of numerical simulation and microseismic monitoring reveals the damage mechanisms in the right bank slope of Dagangshan hydropower station during the impoundment process.

Table 3 Safety factor values

Stage ID	Safety factor					
	Group 1	Group 2	Group 3	Group 4	Group 5	Average
0 (no impoundment)	1.18	1.18	1.17	1.18	1.18	1.18
1	1.16	1.16	1.16	1.16	1.16	1.16
2	1.12	1.12	1.13	1.12	1.12	1.12
3	1.11	1.11	1.11	1.11	1.11	1.11
4	1.10	1.10	1.10	1.10	1.10	1.10

Fig. 14 Variation of the slope safety factor and the monitored microseismic event energy during impoundment
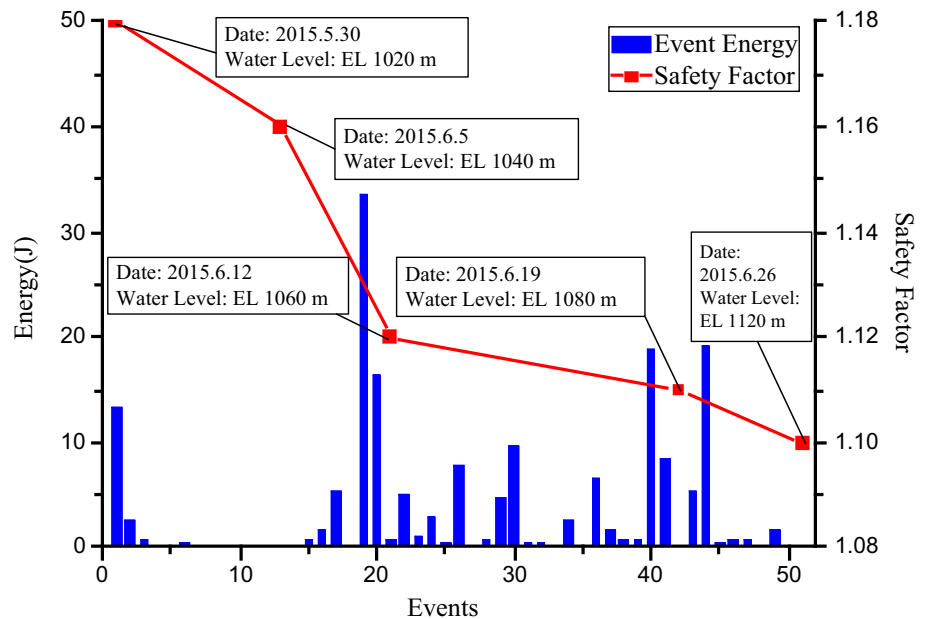
The stability of the right bank slope during the reservoir impounding process is evaluated using a 3D finite element modelling that considers the effects of progressive microseismic damage. The safety factor of the slope decreases as the water level rises during the impoundment process, with an abrupt decrease in the safety factor observed at low water levels due to the release of a large amount of microseismic energy. The evolution of the safety factor reflects the progressive decrease in slope stability. The safety factor of the slope obtained from the 3D finite element modelling that incorporates progressive microseismic damage is 1.10, indicating that the right bank slope at Dagangshan hydropower station is generally stable during reservoir impounding. Progressive microseismic damage considers gradual damage and continuous changes that occur within the slope during the impoundment process. The 3D finite element modelling, which considers the effects of progressive microseismic damage, can reflect changes in the slope during impoundment and can be used to appropriately evaluate the safety factor and slope stability.

References

Adhikary D, Dyskin A (2007) Modelling of progressive and instantaneous failures of foliated rock slopes. Rock Mech Rock Eng 40:349–362

Barla G, Paronuzzi P (2013) The 1963 Vajont landslide: 50th anniversary. Rock Mech Rock Eng 46:1267

Bjerrum L (1967) Progressive failure in slopes of over consolidated plastic clay soil. J Mech Found Div ASCE 93:3–50

Borja RI, White JA (2010) Continuum deformation and stability analyses of a steep hillside slope under rainfall infiltration. Acta Geotech 5:1–14

Ca Tang, Li L, Xu N, Ma K (2015) Microseismic monitoring and numerical simulation on the stability of high-steep rock slopes in hydropower engineering. J Rock Mech Geotech Eng 7:493–508

Chen X (2010) Overview of landslides due to reservoir impoundment based on shear strength properties of sliding zone soils. Adv Sci Technol Water Resour 30:77–83 **(in Chinese)**

Chen G, Huang R, Xu Q, Li T, Zhu M (2013) Progressive modelling of the gravity-induced landslide using the local dynamic strength reduction method. J Mt Sci 10:532–540

Cheng H, Zhang H, Zhu B, Shi Y (2012) Finite element analysis of steep excavation slope failure by CFS theory. Earthq Sci 25:177–185

Chowdhury R (1978) Analysis of the vajont slide—new approach. Rock Mech 11:29–38

Dai F, Deng J, Tham L, Law K, Lee C (2004) A large landslide in Zigui County, Three Gorges area. Can Geotech J 41:1233–1240

Eberhardt E, Stead D, Coggan J (2004) Numerical analysis of initiation and progressive failure in natural rock slopes—the 1991 Randa rockslide. Int J Rock Mech Min Sci 41:69–87

Gencer M (1985) Progressive failure in stratified and jointed rock mass. Rock Mech Rock Eng 18:267–292

Gischig V, Preisig G, Eberhardt E (2016) Numerical investigation of seismically induced rock mass fatigue as a mechanism contributing to the progressive failure of deep-seated landslides. Rock Mech Rock Eng 49:2457–2478

Gurocak Z, Alemdag S, Zaman MM (2008) Rock slope stability and excavatability assessment of rocks at the Kapikaya dam site, Turkey. Eng Geol 96:17–27

Hong Y, Hiura H, Shino K, Sassa K, Suemine A, Fukuoka H, Wang G (2005) The influence of intense rainfall on the activity of large-scale crystalline schist landslides in Shikoku Island, Japan. Landslides 2:97–105

Igwe O, Mode W, Nnebedum O, Okonkwo I, Oha I (2014) The analysis of rainfall-induced slope failures at Iva Valley area of Enugu State, Nigeria. Environ Earth Sci 71:2465–2480

Jackson J, McKenzie D (1988) The relationship between plate motions and seismic moment tensors, and the rates of active deformation in the Mediterranean and Middle East. Geophys J Int 93:45–73

Jiao Y, Zhang H, Tang H, Zhang X, Adoko AC, Tian H (2014) Simulating the process of reservoir-impoundment-induced landslide using the extended DDA method. Eng Geol 182:37–48

Kostrov V (1974) Seismic moment and energy of earthquakes, and seismic flow of rock. Phys Solid Earth 1:13–21

Leshchinsky B, Vahedifard F, Koo H-B, Kim S-H (2015) Yumok-jeong Landslide: an investigation of progressive failure of a hillslope using the finite element method. Landslides 12:997–1005

Li L, Tang C, Zhu W, Liang Z (2009) Numerical analysis of slope stability based on the gravity increase method. Comput Geotech 36:1246–1258

Liang Z, Xing H, Wang S, Williams D, Tang C (2012) A three-dimensional numerical investigation of the fracture of rock specimens containing a pre-existing surface flaw. Comput Geotech 45:19–33

Liao Q, Li X, Lee S, Dong Y (2005) Occurrence, geology and geomorphy characteristics and origin of Qianjiangping landslide in Three Gorges Reservoir area and study on ancient landslide criterion. Chin J Rock Mech Eng 24:3146–3153 (in Chinese)

Lin P, Zhou W, Liu H (2015) Experimental study on cracking, reinforcement, and overall stability of the Xiaowan super-high arch dam. Rock Mech Rock Eng 48(2):819–841

Lin P, Liu X, Hu S, Li P (2016) Large deformation analysis of a high steep slope relating to the Laxiwa Reservoir, China. Rock Mech Rock Eng 49:2253–2276

Ma S, Han T, Xu R, Wu J, Zhang J (2014) Effects of intense rainfall on stability of infinite terraced slope. J Cent South Univ 21:1534–1545

Manual AUs (2000) Ansys Inc Modeling, CFX 11

Miao H, Yin K, Li D (2011) Mechanical analysis for progressive failure of debris landslide. J Mt Sci 8:328–335

Parker R, Petley D, Densmore A, Rosser N, Damby D, Brain M (2013) Progressive failure cycles and distributions of earthquake-triggered landslides. Proceedings of the international symposium on earthquake induced landslides, pp 755–762

Pondrelli S, Morelli A, Boschi E (1995) Seismic deformation in the Mediterranean area estimated by moment tensor summation. Geophys J Int 122:938–952

Savage J, Simpson R (1997) Surface strain accumulation and the seismic moment tensor. Bull Seismol Soc Am 87:1345–1353

Tomida N, Sato N, Soda H, Jikan S, Ohmori K, Ohta H (2011) Estimation of rockfill dam behavior during impounding by elasto-plastic model. In: Schleiss AJ, Boes RM (eds) Dams and Reservoirs under Changing Challenges, Taylor and Francis Group, London, pp 27–34

Wang M, Yan E (2007) Study on influence of reservoir water impounding on reservoir landslide. Rock Soil Mech 28:2722 (in Chinese)

Wang LP, Zhang G (2014) Progressive failure behavior of pile-reinforced clay slopes under surface load conditions. Environ Earth Sci 71:5007–5016

Wang F, Wang G, Sassa K, Takeuchi A, Araiba K, Zhang Y, Peng X (2005) Displacement monitoring and physical exploration on the Shuping Landslide reactivated by impoundment of the Three Gorges Reservoir, China. Landslides: risk analysis and sustainable disaster management, pp 313–319

Wang H, Xu W, Xu R, Jiang Q, Liu J (2007) Hazard assessment by 3D stability analysis of landslides due to reservoir impounding. Landslides 4:381–388

Wang F, Zhang Y, Huo Z, Peng X, Wang S, Yamasaki S (2008) Mechanism for the rapid motion of the Qianjiangping landslide during reactivation by the first impoundment of the Three Gorges Dam reservoir, China. Landslides 5:379–386

Wang J, Yao L, Hussain A (2010) Analysis of earthquake-triggered failure mechanisms of slopes and sliding surfaces. J Mt Sci 7:282–290

Wang F, Yin Y, Huo Z, Wang G (2013) Landsliding caused by water level variation in China Three Gorges Reservoir. In: Margottini C, Canuti P, Sassa K (eds) Landslide Science and Practice, vol 6. Springer Berlin, Heidelberg, pp 19–26

William GP, Saurabh P, Steve CS (2008) A new model for effects of impersistent joint sets on rock slope stability. Int J Rock Mech Min Sci 45(2):122–131

Wong LNY, Wu Z (2014) Application of the numerical manifold method to model progressive failure in rock slopes. Eng Fract Mech 119:1–20

Xia M, Ren GM, Zhu SS, Ma XL (2014) Relationship between landslide stability and reservoir water level variation. Bull Eng Geol Environ 74:909–917

Xiang J, Tang H (2011) Failure mechanism study for Fairy-River shore slope in the Three Gorges Reservoir caused by water-impoundment. J Chongqing Jiaotong Univ (Natural Science) 30(A01):700–704 (in Chinese)

Xiao S, Liu D, Hu Z (2007) Study on geomechanical model of Qianjiangping landslide, Three Gorges Reservoir. Rock Soil Mech 28:1459 (in Chinese)

Xie H, Ju Y, Li L (2005) Criteria for strength and structural failure of rocks based on energy dissipation and energy release principles. Chin J Rock Mech Eng 24:3003–3010 (in Chinese)

Xu N, Dai F, Liang Z, Zhou Z, Sha C, Tang C (2014) The dynamic evaluation of rock slope stability considering the effects of microseismic damage. Rock Mech Rock Eng 47:621–642

Yang Q, Ji D, Luan M (2005) Analysis of progressive failure reliability of geogrid-reinforced slopes. Dalian Loging Daxue Xuebao J Dali Univ Technol (China) 45:85–89 (in Chinese)

Yang H, Jian W, Wang F, Meng F, Okeke AC (2013) Numerical simulation of failure process of the Qianjiangping Landslide

triggered by water level rise and rainfall in the Three Gorges Reservoir, China. Progress of geo-disaster mitigation technology in Asia, Environmental Science and Engineering, pp 503–523

Yerro A, Pinyol NM, Alonso EE (2015) Internal progressive failure in deep-seated landslides. Rock Mech Rock Eng 49:1–16

Zhang J, Xu Y, Qi T, Li Z (2005) Mechanism on progressive failure of a faulted rock slope due to slip-weakening. Sci China Ser E Eng Mater Sci 48:18–26

Zhang K, Cao P, Meng J, Li K, Fan W (2014) Modeling the progressive failure of jointed rock slope using fracture mechanics and the strength reduction method. Rock Mech Rock Eng 48:771–785

Zhao H, Ma F, Xu J, Guo J, Yuan G (2014) Experimental investigations of fault reactivation induced by slope excavations in China. Bull Eng Geol Environ 73:891–901

Zhou Q, Zhang G, Liu Y (2013) Prediction of and early warning for deformation and stress in the Xiaowan arch Dam during the first impounding stage. Appl Mech Mater 405–408:2463–2472

Zhou X, Zhao Y, Qian Q (2015) A novel meshless numerical method for modeling progressive failure processes of slopes. Eng Geol 192:139–153

Zhu H, Xu Q, Ding W, Huang F (2011) Experimental study on the progressive failure and its anchoring effect of weak-broken rock vertical slope. Front Archit Civil Eng China 5:208–224